Cancer Research

February 15, 2009 • Volume 69 • Number 4 • Pages 1243–1696

***In Vivo* ORS MRI of $\alpha_v\beta_3$-Targeted Nanoparticles**
Page 1651

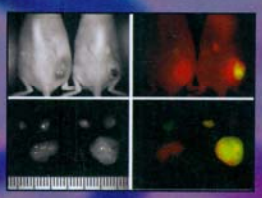

Quenching Near-Infrared Fluorescent Probe Using mAb for Cancer Imaging
Page 1268

***BRMS1* Activates miR-146 and Suppresses Breast Cancer Metastasis**
Page 1279

www.aacrjournals.org

AACR American Association for Cancer Research

In vivo Off-Resonance Saturation Magnetic Resonance Imaging of $\alpha_v\beta_3$-Targeted Superparamagnetic Nanoparticles

Chalermchai Khemtong,[1] Chase W. Kessinger,[1] Jimin Ren,[2] Erik A. Bey,[1] Su-Geun Yang,[1] Jagadeesh Setti Guthi,[1] David A. Boothman,[1] A. Dean Sherry,[2] and Jinming Gao[1]

[1]Department of Pharmacology, Simmons Comprehensive Cancer Center and [2]The Advanced Imaging Research Center, University of Texas Southwestern Medical Center, Dallas, Texas

Abstract

Magnetic resonance imaging is a powerful clinical imaging technique that allows for noninvasive tomographic visualization of anatomic structures with high spatial resolution and soft tissue contrast. However, its application in molecular imaging of cancer has been limited by the lack of sensitivity and detection accuracy in depicting the biochemical expression of these diseases. Here, we combine an ultrasensitive design of superparamagnetic polymeric micelles (SPPM) and an off-resonance saturation (ORS) method to enhance the imaging efficacy of tumor biomarkers *in vivo*. SPPM nanoparticles encoded with cyclic(RGDfK) were able to target the $\alpha_v\beta_3$-expressing microvasculature in A549 non–small cell lung tumor xenografts in mice. ORS greatly improved tumor detection accuracy over the conventional T_2*-weighted method by its ability to turn "ON" the contrast of SPPM. This combination of ORS imaging with a tumor vasculature–targeted, ultrasensitive SPPM design offers new opportunities in molecular imaging of cancer. [Cancer Res 2009;69(4):1651–8]

Introduction

New contrast mechanisms and imaging probes have been actively pursued for cancer molecular imaging by magnetic resonance imaging (MRI). Chemical exchange saturation transfer (CEST; ref. 1), a new contrast mechanism where a radiofrequency irradiation is used to noninvasively saturate agent protons that exchange with water, has led to many novel molecular imaging agents to monitor pH (2), glucose (3), and gene expression (4). For most CEST probes and conventional T_1 contrast agents (e.g., Gd-DTPA), however, their detection limits are above micromolar (μmol/L) concentrations (3, 4), which makes it a considerable challenge to visualize specific disease markers at much lower physiologic concentrations (e.g., <nmol/L). Recently, superparamagnetic nanoparticles [e.g., Fe_3O_4 (5, 6), $MnFe_2O_4$ (7), and FeCo (8)] have received considerable attention as molecular imaging probes with substantially higher molar relaxivities over small molecular MRI agents. Once bound to a targeted marker or after internalization into a cell, superparamagnetic probes can create substantial disturbances in the local magnetic field leading to a rapid dephasing of protons and loss of MR signal intensity. Conventionally, T_2*-weighted (T_2*-w) method serves as the gold standard for the imaging of superparamagnetic probes where a precontrast scan and a postcontrast scan are required to visually detect contrast changes. This method is prone to image artifacts due to B_0 inhomogeneity and is quite limited when a slight position change occurs between MR scans, which can considerably deteriorate the detection accuracy of imaging probes in subtracted images.

In this report, we describe the use of superparamagnetic polymeric micelles (SPPM) in combination with an off-resonance saturation (ORS) method for *in vivo* molecular imaging of cancer (Fig. 1*A*). Polymeric micelles are a new class of self-assembled nanoparticles with a core-shell architecture wherein the hydrophobic core serves as a natural carrier environment for hydrophobic agents and the hydrophilic shell provides particle stabilization and multivalent molecular targeting (9). Clustering of superparamagnetic iron oxide (SPIO) nanoparticles inside the hydrophobic core of a micelle dramatically increased the T_2 relaxivity (e.g., r_2 = 471 Fe mmol/L^{-1}s^{-1} at 1.5 T, >10 times increase over single SPIO particles at the same Fe concentration; ref. 10). Surface functionalization of SPPM by a cyclic(RGDfK) ligand (cRGD) allowed the effective targeting of $\alpha_v\beta_3$ integrins on tumor endothelial cells and subsequent receptor-mediated endocytosis of micelles *in vitro* (11). Here, we use a new ORS method (12) for imaging of cRGD-encoded SPPM in angiogenic tumors in mice. Similar to CEST, the ORS method applies a presaturation pulse that can turn "ON"/"OFF" the probe contrast. Unlike CEST where a specific exchangeable proton frequency is presaturated, the ORS method presaturates at an off-resonance frequency position away from the bulk water. This SPPM-induced ORS contrast is illustrated in Fig. 1*B*. In the absence of SPPM, the presaturation radiofrequency (RF) pulse has little effect on the signal intensity of SPPM-free water (Fig. 1*B, top*); in the presence of SPPM, the RF pulse can saturate a larger volume fraction of water molecules due to proton relaxation by SPPM, which can lead to a considerable decrease in signal intensity (ΔSI, *bottom*). Due to the rapid diffusion of water molecules, ORS contrast can be significantly amplified (12). We illustrate that the ORS method can detect picomolar (10^{-12} mol/L) concentrations of SPPM *in vitro* and show an improved ability to detect angiogenic tumors using cRGD-encoded SPPM probes over traditional T_2*-w imaging method.

Materials and Methods

Production of cRGD-encoded and cRGD-free SPPM. cRGD-encoded and cRGD-free SPPM were prepared according to a previously published procedure (11). Iron contents were determined on a Varian SpectrAA 50 spectrometer (air/acetylene flame). Amino acid quantities in the cRGD-encoded SPPM sample were analyzed by the W.M. Keck Facility,

Note: Supplementary data for this article are available at Cancer Research Online (http://cancerres.aacrjournals.org/).

C. Khemtong and C.W. Kessinger contributed equally to this work.

Requests for reprints: Jinming Gao, Simmons Comprehensive Cancer Center, University of Texas Southwestern Medical Center, 5323 Harry Hines Boulevard, Dallas, TX 35790. Phone: 214-645-6370; Fax: 214-645-6347; E-mail: jinming.gao@utsouthwestern.edu.

©2009 American Association for Cancer Research.

doi:10.1158/0008-5472.CAN-08-3231

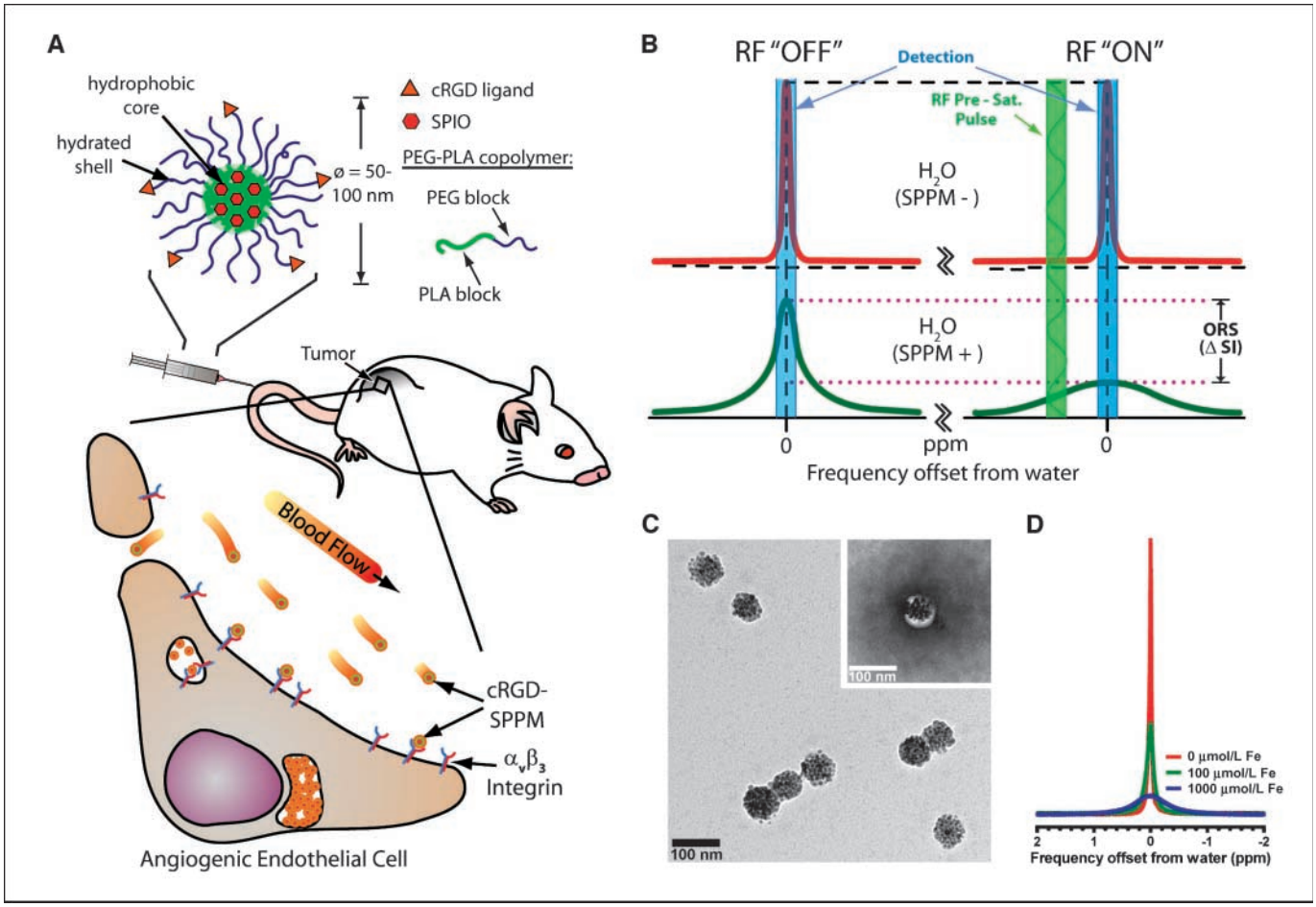

Figure 1. Cancer molecular imaging by cRGD-encoded SPPM and ORS MRI. *A,* schematic illustration of a cRGD-encoded SPPM and its targeting to $\alpha_v\beta_3$-expressing endothelial cells in the tumor vasculature. *B,* mechanism of SPPM-induced ORS contrast. Presaturation RF pulse results in significant decrease in signal intensity (ΔSI) in SPPM(+) H_2O over SPPM(−) H_2O. *C,* TEM image of a representative SPPM sample. *Inset,* a SPPM particle after negative staining with 2% PTA solution. *D,* ^{1}H-NMR (300 MHz) spectra of water containing different concentrations of SPPM (in [Fe]/μmol/L).

Yale University. Micelles were characterized by transmission electron microscopy (TEM) and dynamic light scattering (DLS).

Magnetic resonance imaging. All MRI experiments were conducted on a 4.7 T Inova horizontal scanner (Varian) using a Litz coil (diameter, 4 cm; length, 8 cm; DOTY Scientific, Inc.) at either room temperature (~20°C) for the phantom samples or 37°C for the animal studies. Concentrations of SPPM in the phantoms, presented as molar concentrations of iron, were 0, 2, 5, 10, 20, 50, and 100 μmol/L. Each SPPM solution (100 μL) was added into wells of 5 × 5–well plates. ORS experiments were carried out using a spin-echo (SE) pulse sequence (TR = 2 s; TE = 12 ms) modified by the addition of a frequency-selective Gaussian-shaped presaturation pulse. The phantom and animal studies were RF irradiated at a saturation B_1 power of 3.85 μT for 0.5 s at frequency offsets of 0, ±200, 400, 500, 600, 700, 800, 900, 1,000, 2,000, and 4,000 Hz from bulk water. Reference images were collected using identical settings but without the presaturation pulse. The ORS contrast images were generated by pixel-by-pixel subtraction of the saturation ON image by the reference image. The T_2*-w method was acquired using a gradient echo sequence [TR = 400 ms; TE = 5, 10, and 20 ms; flip angle = 20°]. All MRI images were processed using ImageJ (NIH). The *P* values were calculated using the Student's two-tailed *t* test ($P \leq 0.05$ is considered statistically significant).

Animal studies. All procedures were approved by the Institutional Animal Care and Use Committee at the University of Texas Southwestern Medical Center. A human non–small cell lung cancer A549 xenograft model in athymic female nude mice (18–22 g) was used, with 5×10^6 cells injected s.c. into both flanks. Tumors were allowed to reach adequate size (~200–400 mm^3) before injection of SPPM particles. For intratumoral studies, tumor-bearing mice were sacrificed before scanning to avoid perfusion loss of SPPM nanoparticles. The animals were first imaged by the T_2*-w and ORS methods to obtain the preinjection images. SPPM particles (20 μL, 250 μg Fe/mL) were then directly injected into one tumor and the resulting animals were imaged again to obtain postinjection images. For i.v. studies, cRGD-encoded SPPM, cRGD-free SPPM, and a combination of cRGD-encoded SPPM and free cRGD peptide (18 molar excess) were injected at a dose of 6 mg Fe/kg through the tail vein. During MRI, mice were maintained under anesthesia with 1.5% isoflurane combined with 60:40 oxygen/nitrogen at a flow rate of 500 to 1,000 mL/min delivered to the free-breathing animal via a face mask. Temperature was maintained using a warming blanket with circulating water at 37°C. After MRI, mice were sacrificed and tumor tissues and other organs were harvested for histologic analysis.

Pharmacokinetic analysis. Experiments involving radioactive materials were approved by the Radiation Safety Committee at the University of Texas Southwestern Medical Center. ^{3}H (or T)–labeled cRGD-encoded and cRGD-free SPPMs were prepared from 75% MeO-PEG-PLA-C(O)CT_3 and 25% MAL-PEG-PLA. For the plasma concentration-time experiment, mice bearing A549 tumors were randomly divided into two groups ($n = 4$ for each group) for cRGD-encoded SPPM and cRGD-free SPPM. The mice were injected with SPPM solutions via tail vein. Blood was collected at 1 min and 1, 2, 4, 8, 12, and 24 h after the injection. Plasma was isolated from RBCs by centrifugation at 1,000 rpm for 10 min. The plasma was subsequently mixed with a tissue solubilizer solution (1 mL, BTS-450; Beckman) at room temperature for 5 h followed by addition of a liquid scintillation mixture

(10 mL, Ready Organic, Beckman) for 12 h. Amount of radioactive isotope was measured by a liquid scintillation counter (Beckman LS 6000 IC). Biodistribution of SPPM particles in tumor and other tissues was performed in a separate group of A549 tumor-bearing mice (n = 3 for each SPPM group). Three formulations were examined: cRGD-encoded SPPM, cRGD-free SPPM, and cRGD-encoded SPPM coinjected with free cRGD (18 molar excess). One hour after SPPM injection, mice were perfused with PBS buffer (~30 mL). Dissected organs were weighed, homogenized, and treated with scintillation mixtures. The SPPM distribution in different organs/tissues was calculated as the percentage of injected dose per gram of tissue (%ID/g).

Prussian blue staining. Tumors were fixed in 10% formalin and cryoprotected with 10% and 18% sucrose solutions. Tissues were then snap frozen in OCT medium and sectioned at 8 μm. For Prussian blue staining, sections were rinsed in distilled water and then incubated in a 1:1 solution of 10% aqueous solution of potassium ferrocyanide and 20% hydrochloric acid for 30 min and then rinsed and counterstained with nuclear fast red.

Results

Characterization of SPPM nanoparticles. To achieve the ultrasensitivity of SPPM, we used a high loading density (33 wt%) of SPIO nanoparticles in poly(ethylene glycol)-*block*-poly(D,L-lactide) (PEG-PLA; molecular weights for PEG and PLA blocks are 5 kDa) micelles. Hydrophobic, monodisperse SPIO nanoparticles (9.9 ± 0.4 nm in diameter) were used in these studies (Supplementary Fig. S1). Figure 1*C* shows a bright-field TEM image of a representative sample with each SPPM containing a cluster of SPIO nanoparticles (45 ± 14 SPIO per SPPM, n = 72, ~9×10^5 Fe ions). The inset in Fig. 1*C* shows the same SPPM sample after staining with an aqueous solution of 2% phosphotungstic acid (PTA). Due to their hydrophobic nature, micelle cores were not stained by PTA and hence showed up as white circles encapsulating a cluster of SPIO nanoparticles. The diameter of SPPM particles was 75 ± 11 nm (n = 52) as determined by TEM. Consistent with this analysis, DLS of SPPM solutions showed a single size distribution with an average hydrodynamic diameter of 70 ± 11 nm. The slightly larger micelle diameter estimated by TEM compared with DLS (although not statistically significant) may reflect micelle spreading on the TEM grid during the sample drying process. ^{1}H-nuclear magnetic resonance (NMR; 300 MHz) spectra of aqueous solutions containing different concentrations of SPPM particles are shown in Fig. 1*D*. Significant peak broadening was observed with increasing Fe concentrations. The strong proton relaxation effects of the SPPM nanoparticles provided the physical basis for ORS imaging (Fig. 1*B*).

Surface functionalization of SPPM with cRGD peptide. In a previous publication (13), we showed that ^{1}H-NMR was able to follow the conjugation of cRGD (via the appearance of aromatic protons from D-Phe at δ = 7.4 ppm) to maleimide group (through the disappearance of its vinyl protons at δ = 6.75 ppm after conjugation) on the micelle surface. In this study, we further quantified the amount of cRGD peptide on the SPPM by amino acid analysis. The cRGD-encoded SPPM was dissolved in a strong

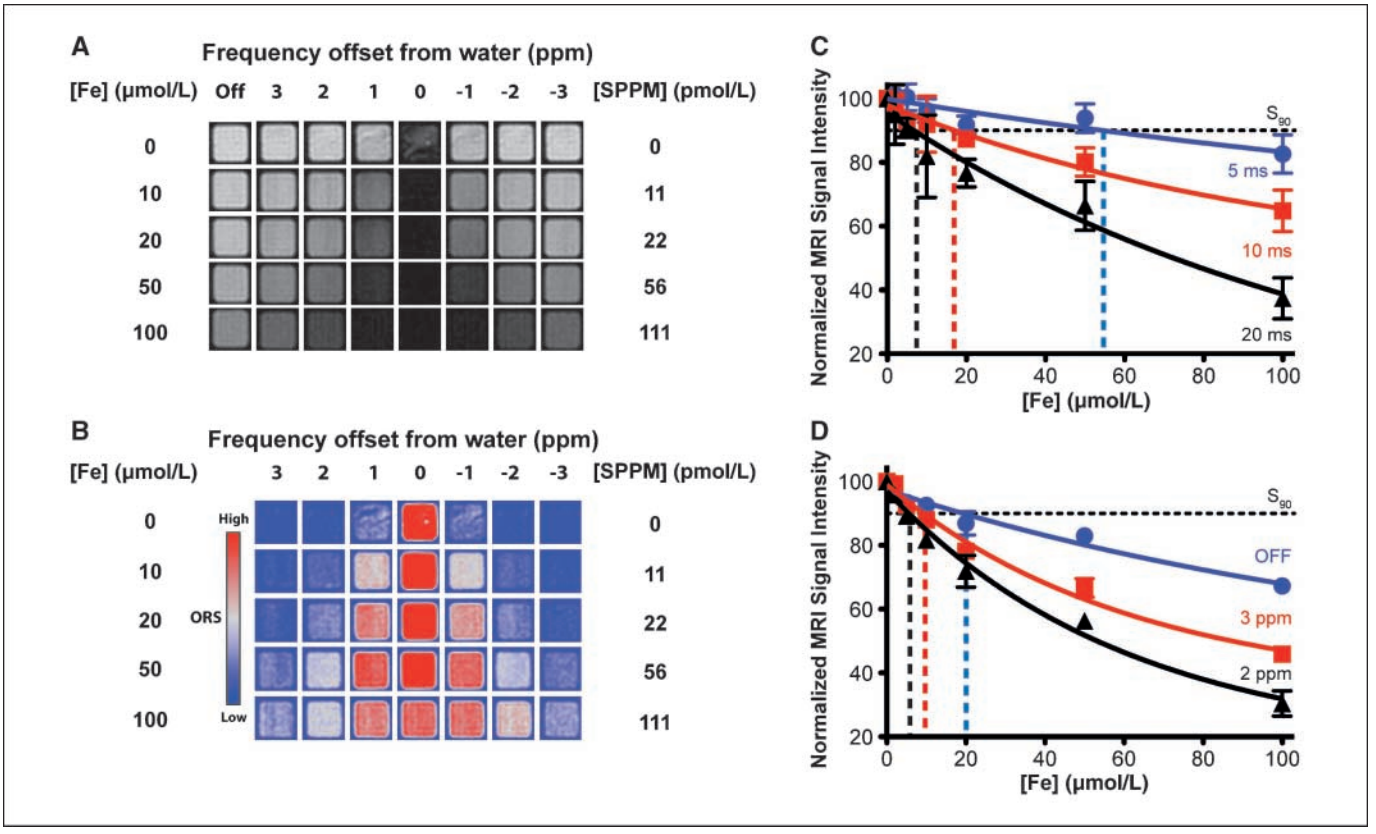

Figure 2. ORS images of SPPM particles in aqueous solution. *A,* ORS images of SPPM solutions at selected saturation frequency offsets (ORS ON) and reference images (ORS OFF) without presaturation. *B,* ORS contrast images obtained by subtracting ORS ON images from the ORS OFF images. The SPPM and Fe concentrations and the frequency offsets from bulk water are indicated. The Fe concentration ([Fe] in μmol/L) was measured by atomic absorption spectroscopy, and SPPM concentration was calculated by dividing [Fe] over the number of Fe ions per SPPM particle (i.e., 9×10^5). ORS images were displayed using the phase in the ImageJ lookup table (LUT). *C* and *D,* normalized signal intensity as a function of SPPM concentrations in [Fe] (μmol/L) by the T_2*-w (*C*) and ORS method (*D*). *Vertical dashed lines,* different S_{90} values under different acquisition conditions for each method.

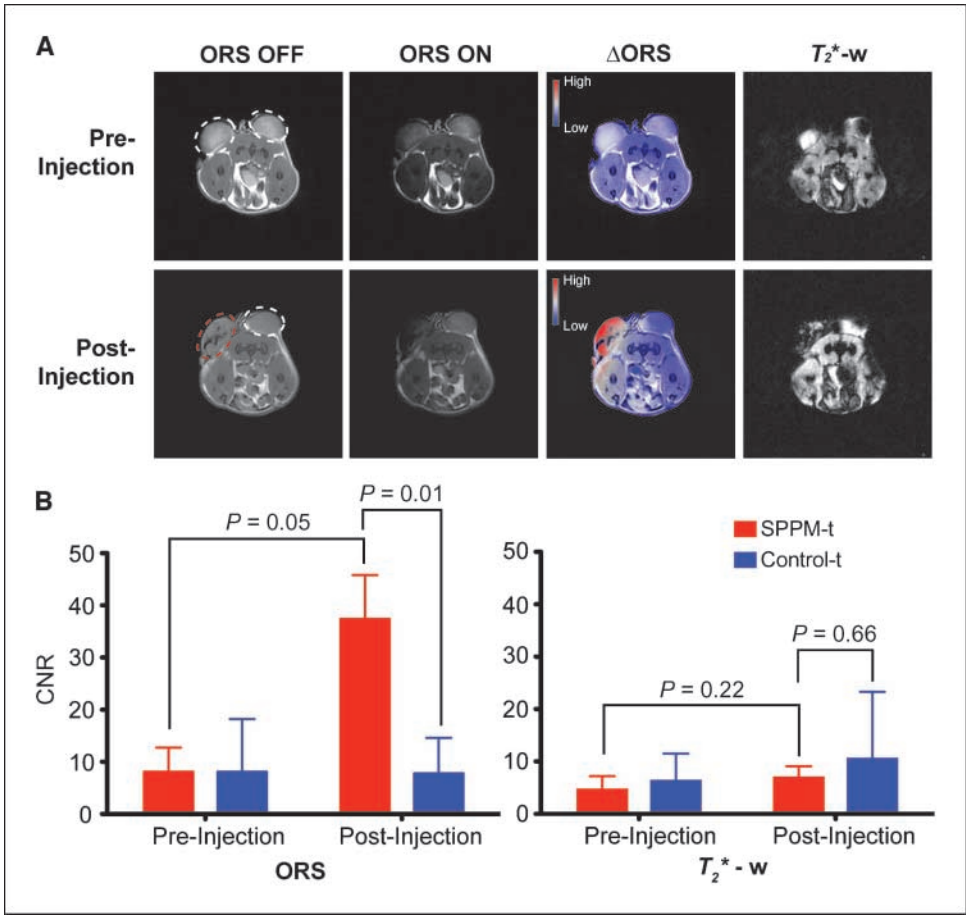

Figure 3. Comparison of ORS and T_2*-w imaging of SPPM nanoprobes (20 μL, 0.25 mg/mL) intratumorally injected inside an A549 tumor xenograft in a mouse. *A,* ORS and T_2*-w images of the transverse section of a representative mouse bearing two tumor xenografts (one for SPPM injection, the other as SPPM-free control) before and after the injection of SPPM. The red dashed circle in the postinjection image indicates the tumor injected with SPPM. The ΔORS images were obtained by pixel-by-pixel subtraction of ORS ON images from ORS OFF images and overlayed with ORS OFF images. The preinjection and postinjection ΔORS images were displayed in the same scale using the phase LUT in ImageJ. The T_2*-w images of the same animal sections were also shown. Mice were sacrificed before scanning to avoid perfusion loss of SPPM nanoparticles. *B,* statistical comparison of CNRs of SPPM-injected versus SPPM-free tumors by the ORS and T_2*-w methods. The *P* values were calculated by the Student's *t* test from three tumor samples under each condition. ORS condition: SE sequence with a 2 ppm ORS B_1 pulse at 3.85 μT for 0.5 s, TR = 2 s, TE = 12 ms; T_2*-w condition: GE sequence, flip angle = 20°, TR = 400 ms, TE = 20 ms. Other imaging conditions are field of view = 50 mm, slice thickness = 2 mm, 128 × 128 matrix, and number of average = 2.

acid (6 N HCl) at an elevated temperature (115°C) to ensure a complete hydrolysis of the peptide and dissociation from the polymer chains. The cRGD density on the surface of SPPM was calculated as a mole percentage of the peptide over that of the PEG-PLA copolymer. The density of the cRGD peptide was 18%, with approximately one in every six polymer chains conjugated with a cRGD peptide.

Imaging of SPPM phantoms. We first investigated the ORS contrast of SPPM particles in aqueous solutions (Fig. 2*A*). The ORS experiment was performed using a SE pulse sequence (TE = 12 ms; TR = 2 s) modified by the addition of a frequency-selective Gaussian-shaped presaturation pulse. RF irradiation was applied using a B_1 of 3.85 μT for 0.5 s at frequency offsets of ±200, 400, 500, 600, 700, 800, 900, 1,000, 2,000, and 4,000 Hz from bulk water. The frequency offsets correspond to ±1, 2, 2.5, 3, 3.5, 4, 4.5, 5, 10, and 20 ppm, respectively (only data from ±1, 2, and 3 ppm were shown in Fig. 2*A*). Reference (ORS OFF) images (Fig. 2*A*) were collected using identical settings but without the presaturation pulse. Figure 2*A* shows that addition of a presaturation RF irradiation at the bulk water resonance frequency darkened the MR intensity for all samples, including SPPM-free water. When a RF pulse was applied at an off-resonance frequency, MR intensity of SPPM-free water increased as the presaturation frequency was moved away from water and became comparable with that without the presaturation pulse. In comparison, in SPPM-containing samples, higher SPPM concentrations and smaller frequency offsets resulted in more pronounced image darkening effects and ORS contrast. To better illustrate ORS contrast, ORS subtraction images were calculated by pixel-by-pixel subtraction of intensities of presaturation images from those of corresponding reference images without presaturation (Fig. 2*B*; also see Supplementary Fig. S2). Two general trends can be observed: (*a*) at the same offset frequency, higher SPPM concentrations yield greater ORS contrast, and (*2*) at equivalent SPPM concentrations, a decrease in the value of the offset frequency leads to greater ORS contrast. It should be noted that it is the value, not the sign, of the saturation-pulse offset that affects the ORS contrast in the phantom samples (i.e., ORS contrast is symmetrical around the bulk water peak, see Fig. 2*B* and Supplementary Fig. S2).

To quantitatively compare the imaging sensitivity between the ORS and T_2*-w methods, we plotted the normalized signal intensity of SPPM sample to water as a function of Fe concentrations (Fig. 2*C* and *D*). Gradient echo sequence was used to acquire the T_2*-w images (flip angle = 20°; TR = 400 ms; TE = 5, 10, and 20 ms). Longer TE times (TE > 30 ms) resulted in considerable image artifacts in T_2*-w images (data not shown) and were not used. The same set of SPPM phantom samples (0, 2, 5, 10, 20, 50, and 100 μmol/L [Fe]) were imaged at four independent times by the T_2*-w and ORS methods, and the SD from each sample was calculated to evaluate the imaging reproducibility. Data show that normalized signal intensity decreased with an increase in SPPM concentrations for both T_2*-w and ORS methods. However, data variation is considerably greater with the T_2*-w method (10–20%; Fig. 2*C*) than the ORS method (2–10%; Fig. 2*D*). We determined the values of S_{90} (SPPM concentration at which signal intensity decreased by 10% from water) from both methods.

In the T_2*-w method, the S_{90} values are 58 ± 21, 18.5 ± 7.5, and 7.5 ± 2.7 pmol/L SPPM (n = 4) for TE at 5, 10, and 20 ms, respectively (Fig. 2*C* shows S_{90} as the vertical dashed lines in [Fe]). In the ORS method, the S_{90} values are 21.3 ± 3.7, 10.1 ± 0.8, and 6.1 ± 0.2 pmol/L SPPM (n = 4) for ORS OFF and ON at 3 and 2 ppm frequency offset, respectively (Fig. 2*D*). It is worth noting that both methods can detect picomolar concentrations of SPPM nanoparticles; however, image reproducibility is much higher in the ORS method than the T_2*-w method. In the following animal studies, we chose to use TE = 20 ms for the T_2*-w method and 2 ppm frequency offset for the ORS method. These two conditions yielded similar sensitivity of SPPM detection in phantoms (e.g., the S_{90} values are 7.5 ± 2.7 and 6.1 ± 0.2 pmol/L for the T_2*-w and ORS methods, respectively).

***In vivo* imaging of SPPM nanoprobes in tumor-bearing mice.** To validate the efficacy of the ORS method for SPPM imaging *in vivo*, we used animals bearing two A549 lung tumor xenografts (~300 mm^3) on each flank of an athymic nude mouse. SPPM nanoparticles (20 μL, 0.25 mg Fe/mL) were directly injected into one tumor (SPPM-t), and the other tumor was used as a SPPM-free control (control-t; Fig. 3*A*). To avoid perfusion loss of SPPM nanoparticles from the tumors, we sacrificed the animal before MRI experiments. After acquisition of ORS and T_2*-w images, signal-to-noise ratio (SNR) was calculated by dividing the mean signal intensity of regions of interest (ROI) such as tumor or muscle tissues over noise. The background noise was calculated as the SD for the largest possible ROI placed outside the animal in the image background. Contrast-to-noise ratio (CNR) was calculated as the contrast difference between the tumor and muscle tissues (CNR_t = SNR_t-SNR_m, where SNR_t and SNR_m are SNRs for tumor and muscle tissues, respectively).

Table 1 shows the values of SNR and CNR from different animals (n = 3) before and after the injection of SPPM. Before SPPM injection, results show that the SNR/CNR values are not statistically significant (P > 0.2) between the two tumor xenografts by either imaging method. More specifically, the $CNR_{SPPM\text{-}t}$ and $CNR_{control\text{-}t}$ are 3.7 ± 2.6 and 6.3 ± 5.2 for the T_2*-w method (P = 0.24) and 8.1 ± 4.6 and 8.1 ± 10.1 for the ORS method (P = 0.99), respectively. These data suggest that the two tumor xenografts have comparable MR properties before SPPM injection. After SPPM injection, ORS data show that the $CNR_{SPPM\text{-}t}$ (37.4 ± 8.4) is significantly higher than the $CNR_{control\text{-}t}$ of SPPM-free tumor control (7.8 ± 6.8; P = 0.01), as well as the same tumor before SPPM injection (8.1 ± 4.6; P = 0.05). In contrast, the CNRs by the T_2*-w method did not show any significant differences (P > 0.2) between the paired comparisons described above (Fig. 3*B*). These data show that the ORS method significantly improves the imaging efficacy of SPPM nanoprobes over the T_2*-w method. This conclusion is supported by images shown in Fig. 3*A* from a representative animal. The ΔORS images before and after SPPM injection clearly showed the ORS contrast in the injected tumors. However, contrast changes in the SPPM-injected tumors by the T_2*-w method are difficult to interpret because considerable changes of signal intensity were also observed in the control tumors and background tissues (Fig. 3*A*; see also discussion below).

Finally, we evaluated the imaging efficacy of A549 tumors by i.v. injection of $\alpha_v\beta_3$-targeted SPPM probes. cRGD-encoded or cRGD-free SPPM were injected (6 mg Fe/kg) into mice bearing A549 tumor xenografts (n = 4 for each SPPM group). The third group of animals was coinjected with cRGD-encoded SPPM and free cRGD peptide (10 mg/kg, 18 molar excess; ref. 14). Our previous studies showed the effective targeting and receptor-mediated endocytosis of cRGD-encoded micelles in $\alpha_v\beta_3$-expressing tumor endothelial SLK cells *in vitro* (11, 13). Here, cRGD-encoded SPPM was used to target the $\alpha_v\beta_3$-expressing angiogenic tumor vasculature *in vivo* (Supplementary Fig. S3 shows $\alpha_v\beta_3$ expression in A549 tumors). One hour after SPPM injection, ORS contrast images showed a clear identification of A549 tumors by cRGD-encoded SPPM probes (Fig. 4*A*). The CNR of the tumor over background muscle tissue was 10.7 ± 3.0 (n = 4; Fig. 4*B*). Prussian blue staining of cRGD-encoded SPPM-treated tumor tissues showed SPPM closely associated with the $\alpha_v\beta_3$ expressing tumor vasculature (Fig. 4*A*). In comparison, cRGD-free SPPM showed accumulation in the tumor parenchyma in a diffusive pattern, likely the result of passive targeting of SPPM to solid tumors through the enhanced permeation and retention effect (Fig. 4*A*; ref. 15). Correspondingly, a smaller CNR (5.1 ± 1.6; n = 4) was observed with the cRGD-free SPPM compared with that of the cRGD-encoded SPPM (10.7 ± 3.0;

Table 1. Comparison of SNR and CNR of SPPM nanoprobes in tumor-bearing mice between T_2*-w and ORS methods

Animal condition	Imaging method	SNR*	CNR†
SPPM preinjection	T_2*-w	15.1 ± 7.0 (SPPM-t)	3.7 ± 2.6 (SPPM-t)
		13.4 ± 2.8 (control-t)	6.3 ± 5.2 (control-t)
		18.8 ± 9.2 (Muscle)	
	ORS	49.4 ± 11.4 (SPPM-t)	8.1 ± 4.6 (SPPM-t)
		43.6 ± 16.6 (control-t)	8.1 ± 10.1 (control-t)
		49.6 ± 16.8 (Muscle)	
SPPM postinjection	T_2*-w	6.9 ± 2.9 (SPPM-t)	6.9 ± 2.2 (SPPM-t)
		24.4 ± 13.6 (control-t)	10.5 ± 12.8 (control-t)
		13.9 ± 4.7 (Muscle)	
	ORS	78.1 ± 21.8 (SPPM-t)	37.4 ± 8.4 (SPPM-t)
		44.2 ± 22.2 (control-t)	7.8 ± 6.8 (control-t)
		40.7 ± 14.3 (Muscle)	

*SNR was calculated as the ratio of mean signal intensity within the ROI of tissues of interest by noise. The SD was obtained from n = 3.
†CNR was calculated as the tumor contrast over the muscle tissue ($CNR = |SNR_t - SNR_m|$). The SD was obtained from n = 3.

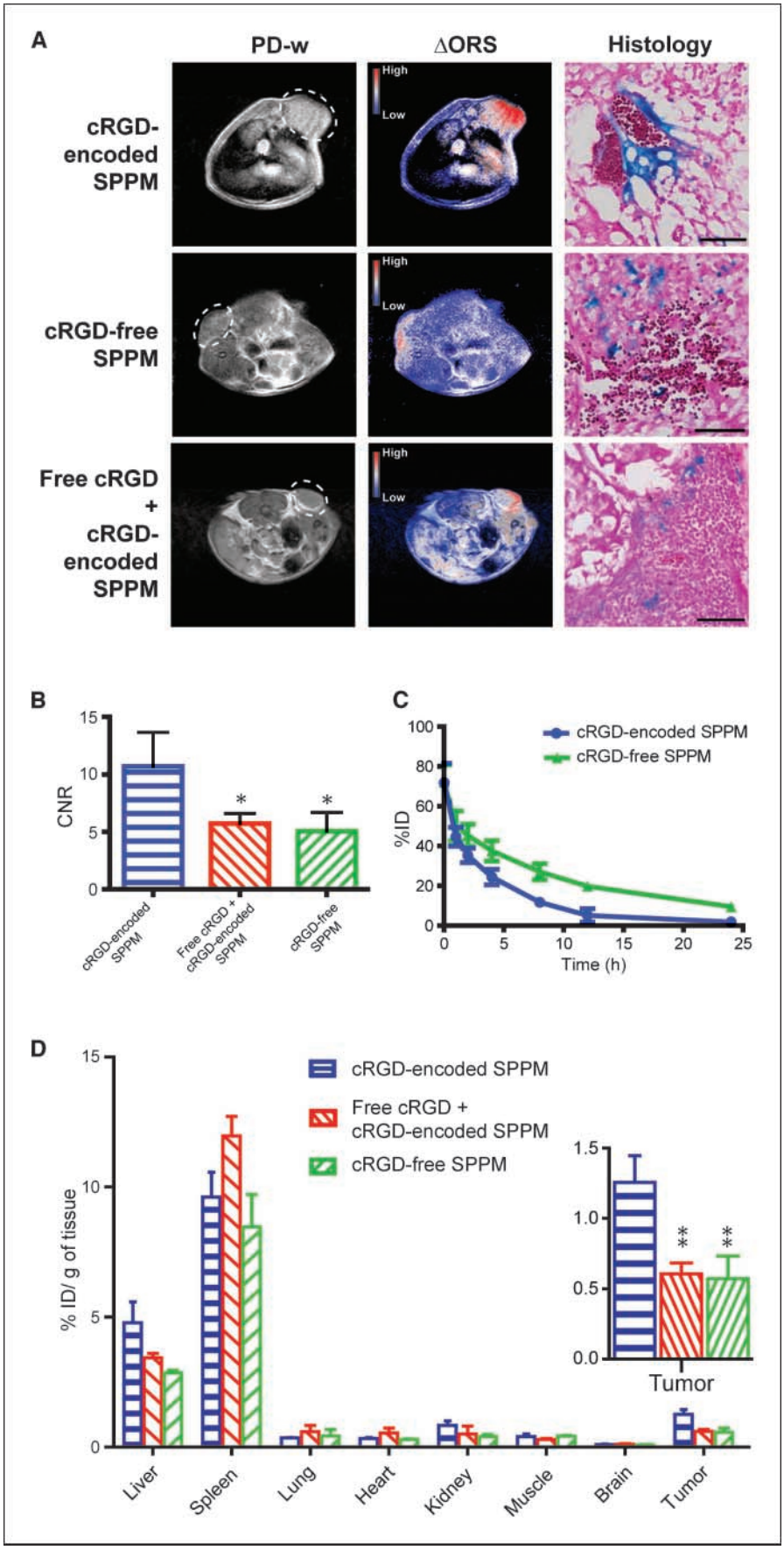

Figure 4. *A, in vivo* ORS imaging of cRGD-encoded SPPM, cRGD-free SPPM, and a mixture of cRGD-encoded SPPM with free cRGD peptide injected i.v. in mice bearing A549 tumor xenografts (6 mg Fe/kg). The ΔORS images showed more accumulation of cRGD-encoded SPPM in A549 tumor xenograft than cRGD-free SPPM and cRGD-encoded SPPM coinjected with free cRGD peptide (18 molar excess). The same phase LUT scale was used in all three ΔORS images for direct contrast comparison. The proton density-weighted (*PD-w*) images were acquired by a SE sequence (TR = 2 s, TE = 9 ms). The same ORS acquisition condition as described in Fig. 3 was used. Histologic sections by Prussian blue staining showed Fe presence from SPPM samples in tumor tissues. The scale bars are 50 μm in all three images. *B,* comparisons of CNRs of ΔORS images of A549 tumor xenograft ($n = 4$) injected with cRGD-encoded SPPM, cRGD-free SPPM, and a mixture of cRGD-encoded SPPM with free cRGD peptide (18 molar excess), respectively. *C,* plasma concentration versus time relationships ($n = 4$ for each SPPM group) for cRGD-encoded SPPM and cRGD-free SPPM. *D,* biodistribution profiles ($n = 3$) of different SPPM formulations (cRGD-encoded SPPM, cRGD-free SPPM, and cRGD-encoded SPPM coinjected with free cRGD) 1 h after i.v. administration. The asterisks (* in *B* and ** in *D, inset*) indicate statistical significance ($P \leq 0.05$) between the SPPM group of interest and cRGD-encoded SPPM based on the Student's *t* test.

$P = 0.02$). To assess the specificity of the cRGD-encoded SPPM for $\alpha_v\beta_3$, blocking experiments, where an excess amount of free cRGD peptide was coinjected with cRGD-encoded SPPM, revealed that tumor accumulation of SPPM decreased, resulting in a decreased CNR (5.3 ± 0.7; $P = 0.02$, compared with that of cRGD-encoded SPPM; Fig. 4*B* and *D*). Prussian blue staining of the tumor section showed a diffusive pattern of SPPM distribution similar to that of cRGD-free SPPM (Fig. 4*A*). These results highlight the efficacy of $\alpha_v\beta_3$-targeted SPPM nanoprobes in the imaging of angiogenic tumor vasculature in A549 tumor xenografts *in vivo*.

Blood circulation half-lives and biodistribution of SPPM. We modified the hydroxyl (-OH) terminal group of MeO-PEG-PLA copolymer with a ^{3}H radioactive moiety [-C(O)CT_3] for the quantitative measurement of SPPM pharmacokinetics *in vivo*. Two groups of animals were injected with cRGD-encoded SPPM and cRGD-free SPPM. Plasma clearance studies showed a two-phase behavior over 24 hours. The plasma half-lives ($t_{1/2,\alpha}$) for the α-phase were 0.34 ± 0.09 and 0.40 ± 0.34 hours for the cRGD-encoded and cRGD-free SPPM ($n = 4$ for each SPPM formulation), respectively. The $t_{1/2,\beta}$ values for the β-phase were 3.9 ± 0.8 and 9.2 ± 0.8 hours for the cRGD-encoded and cRGD-free SPPM ($n = 4$), respectively (Fig. 4*C*).

To corroborate ORS imaging data, we performed biodistribution studies of different SPPM samples 1 hour after i.v. administration of the SPPMs. Spleen (~10% ID/g) and liver (~4% ID/g) were the primary organs for SPPM uptake (Fig. 4*D*). It is important to note that cRGD-encoded SPPM accumulated significantly more in tumors than in the lung, muscle, and brain (Fig. 4*D*). Moreover, tumor uptake of cRGD-encoded SPPM (1.3 ± 0.3% ID/g; $n = 3$) was significantly higher than that of cRGD-free SPPM (0.6 ± 0.3% ID/g; $n = 3$). The coinjection of the free cRGD peptide decreased tumor accumulation of cRGD-encoded SPPM (0.6 ± 0.1% ID/g; $n = 3$).

Discussion

Compared with optical and nuclear imaging methods, the lack of imaging sensitivity is a major limitation for MRI in molecular imaging applications (16). Conventional small molecular T_1 agents (e.g., Gd-DTPA) or new CEST probes [e.g., Eu-DOTA-4AmCE (17)] have limited sensitivity of detection (>μmol/L), which makes it difficult to image specific tumor markers at low physiologic concentrations (<nmol/L). Superparamagnetic nanoparticles (e.g., Fe_3O_4) have shown significantly improved sensitivity due to their strong perturbation to the local magnetic field. Currently, clinically used superparamagnetic agents are synthesized by aqueous precipitation of $FeCl_2$ and $FeCl_3$ in the presence of a dextran polymer (e.g., Feridex). This method yields a variable size distribution of iron oxide nanoparticles (2–20 nm) and the loading of iron oxide per nanoparticle is low (18). Compared with the Fe_3O_4-dextran system, our SPPM design had several distinctive advantages. First, the size distribution of Fe_3O_4 nanoparticles was monodisperse (e.g., 9.9 ± 0.4 nm in diameter), which minimized variability between Fe_3O_4 nanoparticles. Second, clustering of highly compacted Fe_3O_4 particles inside micelle core considerably increased MR relaxivity. Previous study showed that over 10 times enhancement in T_2 relaxivity per Fe was achieved when clustered Fe_3O_4 particles were loaded inside each micelle (10). Third, high loading of Fe_3O_4 (e.g., 33 wt% in this study) effectively increased Fe content per micelle nanoparticle. Combination of increased molar relaxivity and high Fe loading per particle resulted in considerably increased sensitivity of SPPM probes. Indeed, results from this study showed detection of picomolar concentrations of SPPM nanoparticles in phantom samples by MRI. Moreover, the SPPM samples showed superb stability with long storage shelf-lives. These nanoparticles do not aggregate at 4°C even after 1 month of storage in PBS solution. DLS measurements also showed that particle size (~70 nm in diameter) did not change over this time period.

Pharmacokinetic studies showed that SPPM formulations had prolonged blood circulation times, which should allow for effective tumor targeting by the cRGD-encoded SPPM. Both cRGD-encoded and cRGD-free SPPM formulations had comparable α-phase plasma half-lives ($t_{1/2,\alpha}$) at 0.34 ± 0.09 and 0.40 ± 0.34 hours, respectively. However, cRGD-free SPPM showed slower clearance in the β-phase as represented by longer $t_{1/2,\beta}$ (9.2 ± 0.8 hours) than cRGD-encoded SPPM (3.9 ± 0.8 hours). We attribute this variation to the different functionalization of peptides (i.e., cRGD versus Cys) on the SPPM surface. Because the ORS imaging study was performed 1 hour after SPPM injection, we do not anticipate that the different $t_{1/2,\beta}$ values will have a strong influence on the ORS contrast in the current study. Biodistribution studies showed relatively high accumulations of SPPM in the liver and spleen, which are commonly observed for nanoparticles *in vivo* (19). In comparison, SPPM accumulations in other major organs, such as lung, brain, muscle, and kidney, were minimal. More importantly, tumor accumulation of cRGD-encoded SPPM was significantly higher than that of cRGD-free SPPM and cRGD-encoded SPPM coinjected with free cRGD (Fig. 4*D*).

Currently, the T_2*-w method is the gold standard for imaging superparamagnetic nanoparticles. Due to the strong magnetization and field perturbation by the superparamagnetic nanoparticles, the T_2*-w method provides a much higher sensitivity for SPIO agents over conventional T_1 agents (e.g., Gd-DTPA). Despite this advantage, T_2*-w imaging suffers from several major limitations in molecular imaging applications. First, in T_2*-w imaging, significant signal loss can arise due to B_0 inhomogeneity, magnetic susceptibility, or spin-spin couplings. This will lead to signal variations that are independent of the superparamagnetic probes. For example, the preinjection T_2*-w image (Fig. 3*A*) showed considerably different image contrast (tumor ROI analyses showed 2.1 ± 1.2 and 1.2 ± 0.9 for the SPPM-t and control-t, respectively) between the two tumor xenografts in the same mouse before SPPM injection. After SPPM injection, the control tumor (SPPM-free) showed a relative increase in signal intensity (1.7 ± 1.1) compared with its preinjection image (1.2 ± 0.9). Such signal variations can greatly complicate the interpretation of preinjection and postinjection images to identify SPPM contrast on an individual animal basis. Second, T_2* method is also sensitive to different magnetic susceptibility caused by air/tissue or hard/soft tissue interface present in internal organs. These phenomena give rise to signal distortion and can also complicate image analysis. Lastly, identification of SPIO requires a precontrast scan for image subtraction from a postcontrast scan. Small changes of animal positions can easily decrease the spatial resolution (>mm) for tumor detection. Compounded with the variations in signal intensity between the scans, the quality and accuracy of contrast images can be considerably deteriorated in subtracted images.

The ORS method overcomes the above limitations and offers many advantages. The most exciting aspect of ORS is its ability to turn ON the contrast of the SPPM probes after the contrast agents are injected. This ability greatly increases the imaging accuracy in detecting contrast changes in targeted tissues while saving the

need of a precontrast scan as in the T_2*-w method. Because ON and OFF imaging can be performed subsequently without the moving of the imaging subject, pixel-by-pixel subtraction between these images can be performed to provide the maximal spatial resolution in contrast images. In this case, the intrinsic resolution of MRI (e.g., ~100 μm for the 4.7 T scanner in the current study) can be maintained in the ORS contrast images (e.g., Figs. 3 and 4). In contrast, it is impossible to perform accurate pixel-by-pixel subtractions between preinjection and postinjection images in T_2*-w method. It is also interesting to note that although the current acquisition conditions with T_2*-w and ORS methods allowed for similar sensitivities (e.g., S_{90}) in phantom studies, results from animal studies showed significantly improved SNR/CNR by the ORS method for SPPM detection than the T_2*-w method (Table 1; Fig. 3). This improvement indicates that complex physiologic environments may introduce more signal variations in T_2*-w images than the ORS images.

One consideration in using the ORS method is that the ORS imaging protocol also introduces contrast effects by magnetization transfer (MT). The MT effect is dependent on cross-relaxation and/or chemical exchange between the "free" water and macromolecule-associated or "immobile" water (20–22), whereas ORS effect primarily relies on the diffusion of water molecules among different compartments that are defined by magnetic field isosurfaces (12). Our current study allows for a preliminary estimation of MT and ORS effects on SPPM contrast. The CNR for the SPPM-injected tumor is 37.4 ± 8.4 (n = 3), which includes the compounded effects from both ORS and MT. The CNR for the SPPM-free tumors from the same animal is 7.8 ± 6.8, where the SPPM-induced ORS contribution is absent. The significantly higher CNR (P = 0.01) from SPPM-injected tumors suggests that ORS contrast can be effectively detected over the MT contrast. Precautions need to be taken when imaging lower concentrations of SPPM in tumor tissues when the contribution from MT effect becomes significant. Further studies are necessary to quantitatively evaluate the contributions of MT- and/or ORS-based effects on the detection of SPPM.

In conclusion, these studies show the synergy of ultrasensitive SPPM design and ORS method for molecular imaging of cancer, and in particular, non–small cell lung cancer. Phantom studies show detection limit at picomolar (10^{-12} mol/L) concentrations of SPPM nanoprobes, making them comparable in sensitivity with nuclear imaging probes. Results from the animal studies support our hypothesis that ORS method can significantly increase the contrast sensitivity and detection accuracy of SPPM particles in tumor tissues over the conventional T_2*-w method. After i.v. injection, $\alpha_v\beta_3$-targeted SPPM nanoprobes show significantly increased ORS imaging contrast in A549 tumors over the nontargeted SPPM. Pharmacokinetic studies showed prolonged blood circulation times of SPPM nanoparticles and verified the $\alpha_v\beta_3$-dependent targeting specificity by the cRGD-encoded SPPM. The combination of ORS imaging with cancer-targeted SPPM nanoparticles offers new opportunities in detecting biochemical markers at early stages of tumor development.

Disclosure of Potential Conflicts of Interest

No potential conflicts of interest were disclosed.

Acknowledgments

Received 8/20/2008; revised 10/21/2008; accepted 11/10/2008; published OnlineFirst 02/03/2009.

Grant support: NIH grants EB005394 and CA129011 (J. Gao), CA102792 (D.A. Boothman), and CA15531 and CA126608 (A.D. Sherry); Robert A. Welch Foundation AT-584 (A.D. Sherry); and Department of Defense Breast Cancer Research Program Multidisciplinary Postdoctoral Award W81XWH-06-1-0751 (C. Khemtong).

The costs of publication of this article were defrayed in part by the payment of page charges. This article must therefore be hereby marked *advertisement* in accordance with 18 U.S.C. Section 1734 solely to indicate this fact.

This is article CSCN028 from the Program in Cell Stress and Cancer Nanomedicine, Simmons Comprehensive Cancer Center, University of Texas Southwestern Medical Center.

References

1. Ward KM, Aletras AH, Balaban RS. A new class of contrast agents for MRI based on proton chemical exchange dependent saturation transfer (CEST). J Magn Reson 2000;143:79–87.
2. Aime S, Delli Castelli D, Terreno E. Novel pH-reporter MRI contrast agents. Angew Chem Int Ed Engl 2002;41:4334–6.
3. Zhang S, Trokowski R, Sherry AD. A paramagnetic CEST agent for imaging glucose by MRI. J Am Chem Soc 2003;125:15288–9.
4. Gilad AA, McMahon MT, Walczak P, et al. Artificial reporter gene providing MRI contrast based on proton exchange. Nat Biotechnol 2007;25:217–9.
5. Bulte JWM, Kraitchman DL. Iron oxide MR contrast agents for molecular and cellular imaging. NMR Biomed 2004;17:484–99.
6. Thorek DLJ, Chen A, Czupryna J, Tsourkas A. Superparamagnetic iron oxide nanoparticle probes for molecular imaging. Ann Biomed Eng 2006;34:23–38.
7. Lee JH, Huh YM, Jun Y, et al. Artificially engineered magnetic nanoparticles for ultra-sensitive molecular imaging. Nat Med 2007;13:95–9.
8. Seo WS, Lee JH, Sun X, et al. FeCo/graphitic-shell nanocrystals as advanced magnetic-resonance-imaging and near-infrared agents. Nat Mater 2006;5:971–6.
9. Sutton D, Nasongkla N, Blanco E, Gao J. Functionalized micellar systems for cancer targeted drug delivery. Pharm Res 2007;24:1029–46.
10. Ai H, Flask C, Weinberg B, et al. Magnetite-loaded polymeric micelles as ultrasensitive magnetic-resonance probes. Adv Mater 2005;17:1949–52.
11. Nasongkla N, Bey E, Ren J, et al. Multifunctional polymeric micelles as cancer-targeted, MRI-ultrasensitive drug delivery systems. Nano Lett 2006;6:2427–30.
12. Zurkiya O, Hu X. Off-resonance saturation as a means of generating contrast with superparamagnetic nanoparticles. Magn Reson Med 2006;56:726–32.
13. Nasongkla N, Shuai X, Ai H, et al. cRGD-functionalized polymer micelles for targeted doxorubicin delivery. Angew Chem Int Ed Engl 2004;43:6323–7.
14. von Wallbrunn A, Holtke C, Zuhlsdorf M, Heindel W, Schafers M, Bremer C. *In vivo* imaging of integrin $\alpha_v\beta_3$ expression using fluorescence-mediated tomography. Eur J Nucl Med Mol Imaging 2007;34:745–54.
15. Maeda H, Sawa T, Konno T. Mechanism of tumor-targeted delivery of macromolecular drugs, including the EPR effect in solid tumor and clinical overview of the prototype polymeric drug SMANCS. J Control Release 2001;74:47–61.
16. Weissleder R, Pittet MJ. Imaging in the era of molecular oncology. Nature 2008;452:580–9.
17. Zhang SR, Merritt M, Woessner DE, Lenkinski RE, Sherry AD. PARACEST agents: modulating MRI contrast via water proton exchange. Acc Chem Res 2003;36:783–90.
18. Sun SH, Zeng H, Robinson DB, et al. Monodisperse MFe_2O_4 (M = Fe, Co, Mn) nanoparticles. J Am Chem Soc 2004;126:273–9.
19. Torchilin VP. Multifunctional nanocarriers. Adv Drug Deliv Rev 2006;58:1532–55.
20. Wolff SD, Balaban RS. Magnetization transfer contrast (MTC) and tissue water proton relaxation *in vivo*. Magn Reson Med 1989;10:135–44.
21. Henkelman RM, Huang XM, Xiang QS, Stanisz GJ, Swanson SD, Bronskill MJ. Quantitative interpretation of magnetization transfer. Magn Reson Med 1993;29:759–66.
22. Morrison C, Henkelman RM. A model for magnetization transfer in tissues. Magn Reson Med 1995;33:475–82.